Nafar Dastgerdi, J.; Sheibanian, F.; Remes, H.; Lehto, P.; Hosseini Toudeshky, H.

Numerical modelling approach for considering effects of surface integrity on micro-crack formation

Published in:
Journal of Constructional Steel Research

DOI:
10.1016/j.jcsr.2020.106387

Published: 01/12/2020

Document Version
Publisher's PDF, also known as Version of record

Journal of Constructional Steel Research 175 (2020) 106387

Contents lists available at ScienceDirect

Journal of Constructional Steel Research

Numerical modelling approach for considering effects of surface integrity on micro-crack formation

J. Nafar Dastgerdi [a,b,*], F. Sheibanian [a], H. Remes [b], P. Lehto [b], H. Hosseini Toudeshky [a]

[a] Department of Aerospace Engineering, Amirkabir University of Technology, 424 Hafez Avenue, Tehran, Iran
[b] Department of Mechanical Engineering, Aalto University school of Engineering, P.O. Box 14300, Aalto, FIN-00076 Espoo, Finland

ARTICLE INFO

Article history:
Received 12 August 2020
Received in revised form 24 September 2020
Accepted 26 September 2020
Available online xxxx

Keywords:
Surface roughness
Residual stresses
Finite element method
Micro-crack formation

ABSTRACT

This work studies the simultaneous effects of surface roughness and residual stress on the micro-crack formation under peak load conditions. The manufacturing process of e.g. steel components influences the surface topography and the material microstructure. These changes affect the surface integrity, which in turn define the component's mechanical properties such as fatigue strength. This paper introduces an efficient finite-element based approach to analyze the influence of surface roughness, residual stress, and microstructural composition on micro-crack formation mechanism during monotonic peak load. The proposed approach combines surface roughness profiles, a ductile fracture criterion and a layer-wise residual stress definition for an approach that is suitable for surface integrity analysis. An inverse numerical-experimental approach is presented for the calibration of the ductile fracture criterion under different stress states. The developed approach is applied to a sandblasted S690 high strength steel, in which the surface integrity has been altered by the manufacturing process. The possibility of crack initiation in the vicinity of critical micro notches is investigated, and the influence of surface roughness and residual stresses is studied. The proposed modelling principles and calibration approach can be employed for other materials and surface profiles.

1. Introduction

The manufacturing process of metal components influences surface integrity which defines the properties of final components, affecting for instance corrosion and fatigue resistance; see e.g. [1–4]. Surface integrity is usually described by several parameters: (i) a geometrical parameter i.e. surface topography, (ii) a mechanical parameter i.e. residual stress, and (iii) a metallurgical parameter i.e. microstructural composition. These parameters vary depending on the used manufacturing methods and environmental conditions [5–7]. Surface integrity has been shown to be one of the most important factors affecting the growth of micro-cracks [8], fatigue loaded components [9], surface protection coatings [10], and corrosion resistance [11].

Most of the previous works [12–15] studied the influence of individual parameters, mainly surface roughness on the fatigue performance of different engineering materials; however, the formation of micro-cracks is often neglected in fatigue strength assessment. The fatigue behaviour is extremely sensitive to surface topography and it has a crucial effect on fatigue life. There is a general conclusion that fatigue strength decreases as the surface roughness increases. Nevertheless, from the fatigue test results of different materials, the degree of effect varies from one material to another [16,17]. Despite considerable advances in understanding the influence of surface roughness on the fatigue performance of different materials, the role of surface roughness on crack initiation and damage mechanism is poorly understood. In particular, the occurrence of peak loads before or during fatigue loading will affect crack initiation and requires further study. Engineering components are subjected to such high peak stresses and overloads during normal operation and especially as single incidents while operating in severe conditions. Moreover, the effects of residual stress and hardness are still unclear while simultaneously considering the impact of surface roughness effect on the ductile fracture and crack formation. Thus, it is crucial to investigate the combined effect of surface integrity parameters on the properties and micro-cracking of engineering components under peak loads.

Ductile fracture is a well-known physical process that leads to the formation of cracks in metals due to the nucleation, growth and coalescence of voids. Research on ductile fracture has addressed several aspects of the ductile fracture process. Many scholars have conducted research on proposing, calibrating and applying the ductile fracture criterion in different engineering practices [18–21]. The modelling of ductile fracture caused by overloads and impact scenarios is well known in crashworthiness analysis [22–24]. For crashworthiness analysis, long cracks are assumed with large scale yielding taking place. For surface integrity analysis on fatigue strength, these assumptions are invalid, as

* Corresponding author.
E-mail address: jairan.nafardastgerdi@aalto.fi (J. Nafar Dastgerdi).

https://doi.org/10.1016/j.jcsr.2020.106387

micro-cracking and localized yielding take place only in the surface layer of the material. The micro-mechanism motivated phenomenological damage models [25–27] can be a potential option for predicting the ductile fracture initiation in engineering applications [28]. However, in the large-scale simulation inevitably the details of the fracture process, such as the crack initiation, propagation and failure mechanisms are lost.

In this study, a new efficient finite-element based approach is introduced to account for the influences of surface roughness and residual stress simultaneously on the micro-cracking mechanism. A micro-mechanism inspired damage indicator model [26] in the space of stress triaxiality and equivalent plastic strain has been employed for damage initiation and micro-crack formation. An inverse numerical-experimental calibration approach is presented to construct a fracture locus suitable for the surface integrity analyses. The influence of the measured residual stress distribution is modelled with a constant temperature based multi-layer approach. The introduced approach is applied for high strength steel ($S_y = 690$ MPa), which has a sandblasted surface to investigate the influences of surface integrity and monotonic overload on the fracture locus and micro-crack formation. The proposed modelling principles and calibration approach can be employed for other materials and surface profiles. Consequently, this study establishes new research on the influence of surface integrity when peak load affects the surface before fatigue loading. The developed modelling approach enables the characterisation of the influence of an initial peak load on the geometrical parameters, residual stress state and crack formation in different engineering materials.

2. Materials and methods

2.1. Material and experimental procedure

2.1.1. Surface geometry measurement

In this study, the sandblasted 690 high strength steel plate specimen, with a plate thickness of 15 mm is selected as an engineering application case. In the used test sample, before sandblasting, the rolled surface is slightly polished by grinding. The hourglass-shaped plate specimen is used similarly to the previous investigation of the surface integrity effects [5,6]. The width of the narrowest cross-section was 30 mm. As shown in [5], this specimen represents a common engineering application, where high surface roughness and compressive residual stress affect the material properties and strength. The size of the surface defects is measured using surface roughness measurements according to SFS-EN ISO 4288 [29]. The measurements were carried out for the rolled plate surface along three different lines, i.e. at the edges and center of the lower left side of the narrow section of the specimen, as illustrated in Fig. 1a. The measured profile is about 12 mm along the line crossing the middle of the specimen (see z-value 3 line in Fig. 1b) to simulate a real-surface roughness with different micro-defects. This profile is then used as a surface model to generate the finite element (FE) geometry.

For further analysis of the sample surface geometry, the samples are investigated using scanning electron microscopy. Before sample preparation, electroless nickel plating is used to retain the surface geometry. The electroless plating bath composition by Cheong et al. [30] is used to deposit a 20–30 μm nickel layer on the specimens. After nickel plating, the samples are cross-sectioned and mounted in an electrically conductive resin. The samples are ground using P180-P2000 grit abrasive papers, followed by polishing with 3-μm and 1-μm diamond paste. The samples are fine-polished with 0.25-μm diamond paste, followed by colloidal silica polishing in a vibratory polisher to minimize the deformation induced by the sample preparation. A Zeiss Ultra 55 field emission scanning electron microscope is used to study the surface geometry using the Secondary Electron signal.

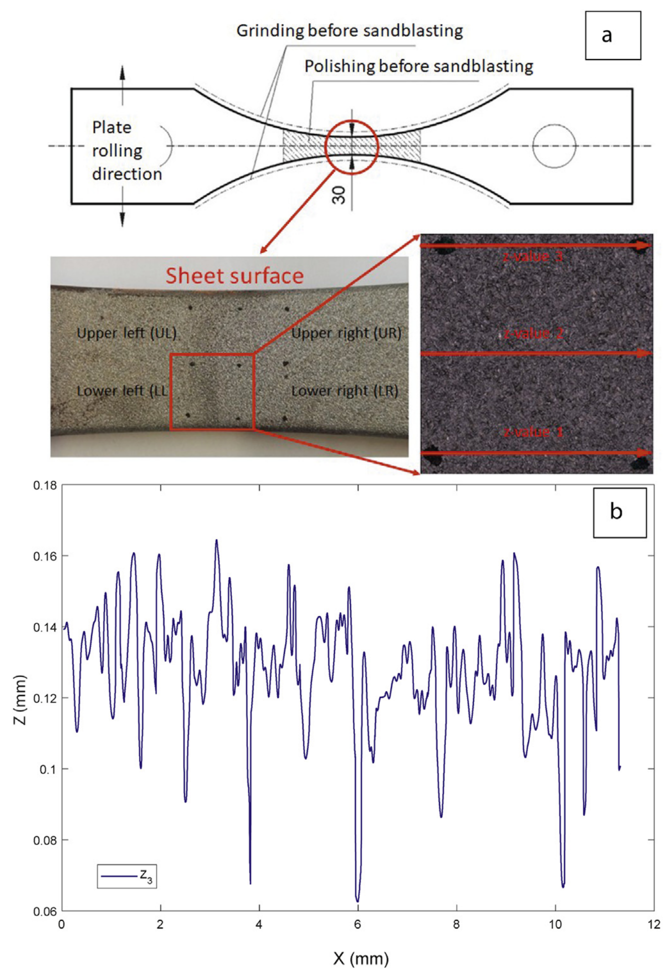

Fig. 1. (a) Defining appropriate region for surface scan and (b) profile of the surface roughness.

2.1.2. Residual stress measurement

Residual stress of the specimen surface is measured using X-ray diffraction with Stresstech X3000 device following EN ISO 15305:2007 [31]. The circular collimator diameter is 3 mm, radiation source was Cr-Kα (30 kV, 6.7 mA), and exposure time 5 s; 6/6 psi tilts are used. For stress evaluation, Young's modulus E of 210 GPa and Poisson ratio ν of 0.3 are used. Measurements are carried out in initial condition, i.e., before any loading. The measurements resulted in an absolute maximum stress value of −80 MPa, which is used in the numerical modelling as a surface residual stress value.

2.1.3. Peak load test

In the peak load test, the test specimen is subjected to compressive loading and then one loading cycle as shown in Fig. 2a. The compressive peak load is defined so that it corresponded to around 1% nominal strain measured from the strain gauges at the middle specimen. The measured load displacement curve is presented in Fig. 2b.

2.2. Numerical simulation

Numerical simulations aim to fully capture the complexity of the local stress-strain fields induced by the surface roughness and to evaluate the influence of residual stress such that they can be introduced into a damage prediction methodology. This section describes the modelling principle, FE meshing and computation procedures for efficient surface

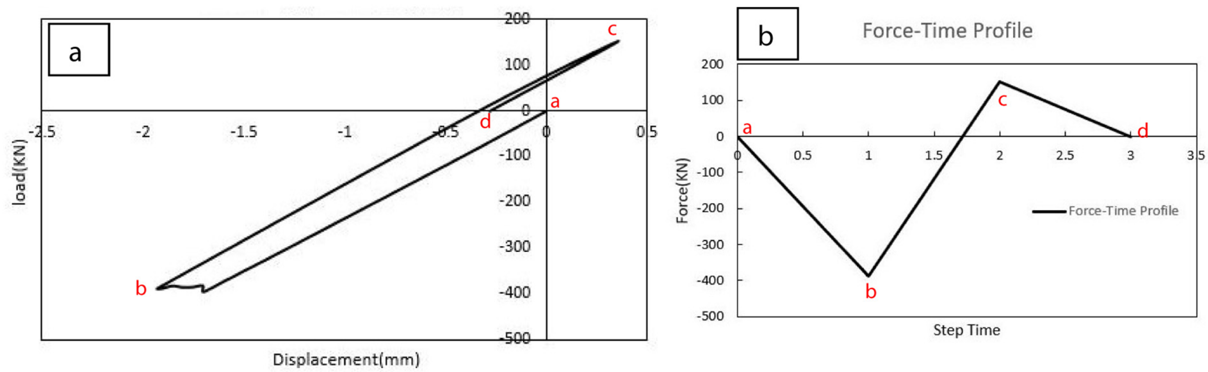

Fig. 2. (a) load–displacement and (b) force control loading condition in one cycle.

integrity analysis. In this study, the numerical simulation is carried out with Abaqus version 6.14.

2.2.1. Surface topography modelling

The sub-model of the highly stressed and critical part of the steel plate is created to accurately model the surface topography. The sub-model size is significantly larger in comparison to the roughness of the surface so that the boundary conditions of the model do not affect the analysis. The boundary conditions for the sub-model are defined from the displacements of the component analysis without a surface topography model. Using a conservative assumption that the depth to length ratio of surface defects is always large, a two-dimensional surface topography model is applied. Fig. 3 presents the two-dimensional FE-model, where the surface geometry is created from the profilometric scan. The final dimension of the model is taken as 31.1 $mm \times 11.28$ $mm \times 15$ mm. Since the surface roughness consists of different micro-notches with sharp tips in some areas, a free mesh cannot provide accurate results. It is important to use the well-defined mesh especially close to the notch tips. Thus, the element mesh is refined in the micro-defect root to be as small as possible being still valid for continuum mechanics. The minimum element size is defined as three times the average grain size of the material, equating to roughly 10 μm for the studied steel. With this approach, the material model is valid for a group of grains instead of the individual grain.

The element type for the micro-defect root area, where material damage and crack formation occur, is four nodes with reduced integration in order to have robust numerical simulation for large strains and geometrical non-linearity.

FE simulations were carried out on the model according to the load and boundary conditions applied in the experimental conditions as shown in Fig. 2ab. Due to the complexity of the surface topology, high local stresses are expected to occur at the surface. To evaluate the effect of local plasticity on the near surface stress fields, elastoplastic behaviour with isotopic hardening is considered. The material model is

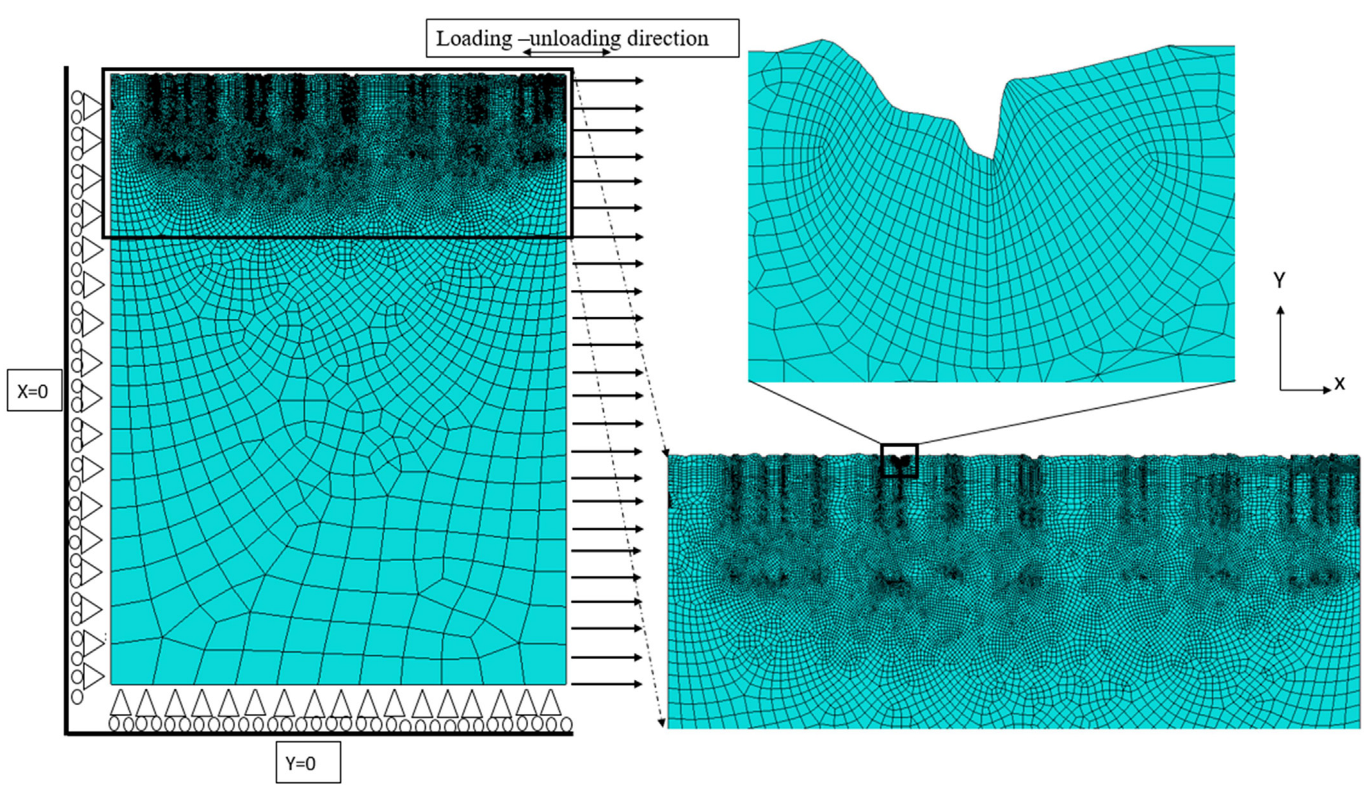

Fig. 3. Two-dimensional real surface topography model and local mesh.

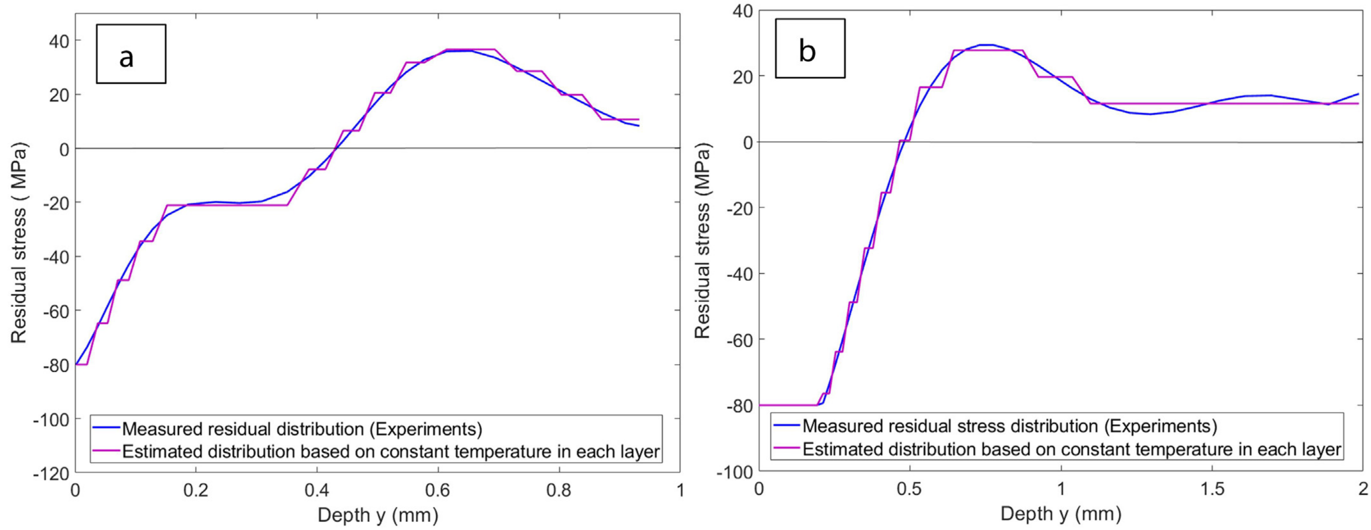

Fig. 4. Continuously estimated residual stress distribution (solid line) and discontinuously estimated residual stress distribution with constant values in each layer (stepwise continuous line) for (a) case 1 and (b) case 2.

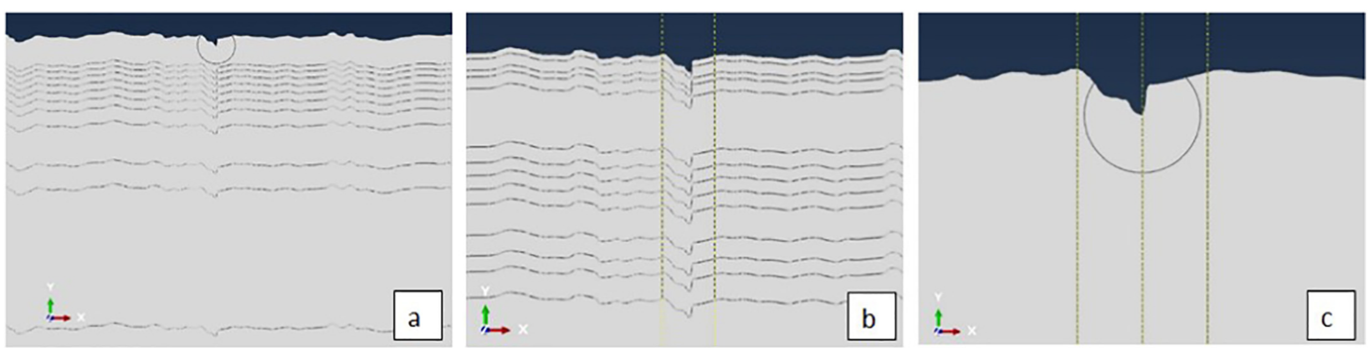

Fig. 5. Different approaches to simulate a known residual stress, (a) layer-wise global distribution as an example for case 2, (b) layer-wise local line distribution for case 1, and (c) continuous local line distribution as an example for case 1.

presented in section 2.3.1. The elastic properties of the materials were described by Young's modulus of E = 210 GPa, Poisson ratio of $\nu =$ 0.3. Von Mises yield criterion was used in the simulations assuming associated plastic flow and isotropic hardening.

2.2.2. Introducing residual stress in FEM

Due to the varied surface topography, the modelling of residual stress requires special attention. Based on the comparison of the different modelling strategies, a layer-wise global modelling approach is proposed in this study. The layer-wise modelling approach can model residual stress fields and consider the effect of varied material properties in the surface layer.

To estimate through-thickness residual stress distributions, the data from the strain-gage hole drilling measurements for sandblasted steel samples were utilized from Ref. [32]. To cover statistical variation in the measurements, two stress distribution cases are studied as shown

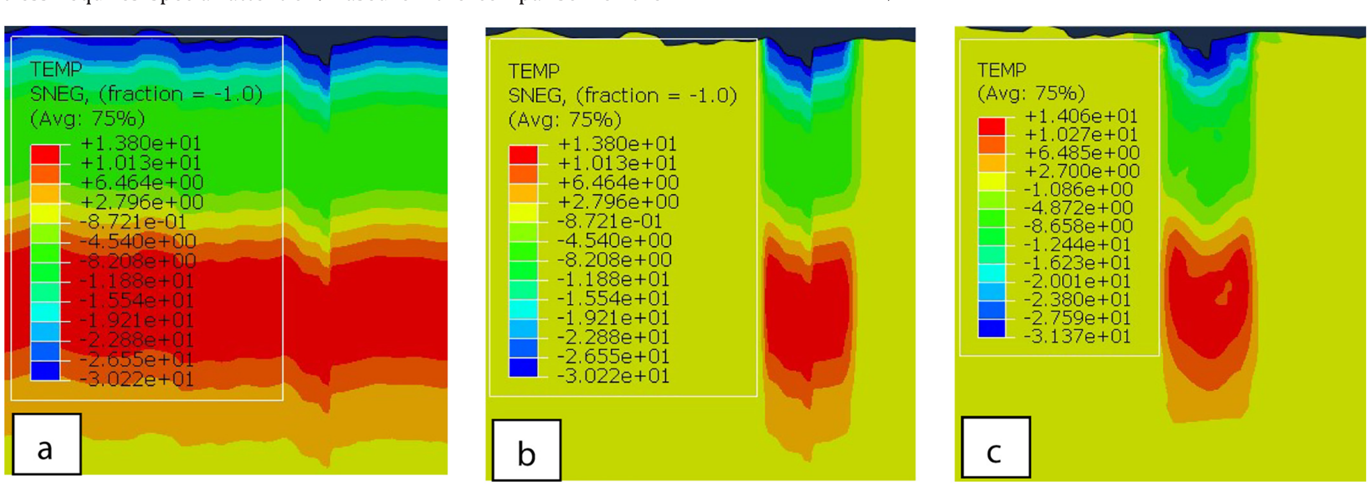

Fig. 6. The applied temperature filed using (a), (b) globally and locally layer-wise approaches, (c) continuous local line approach, respectively for case 1.

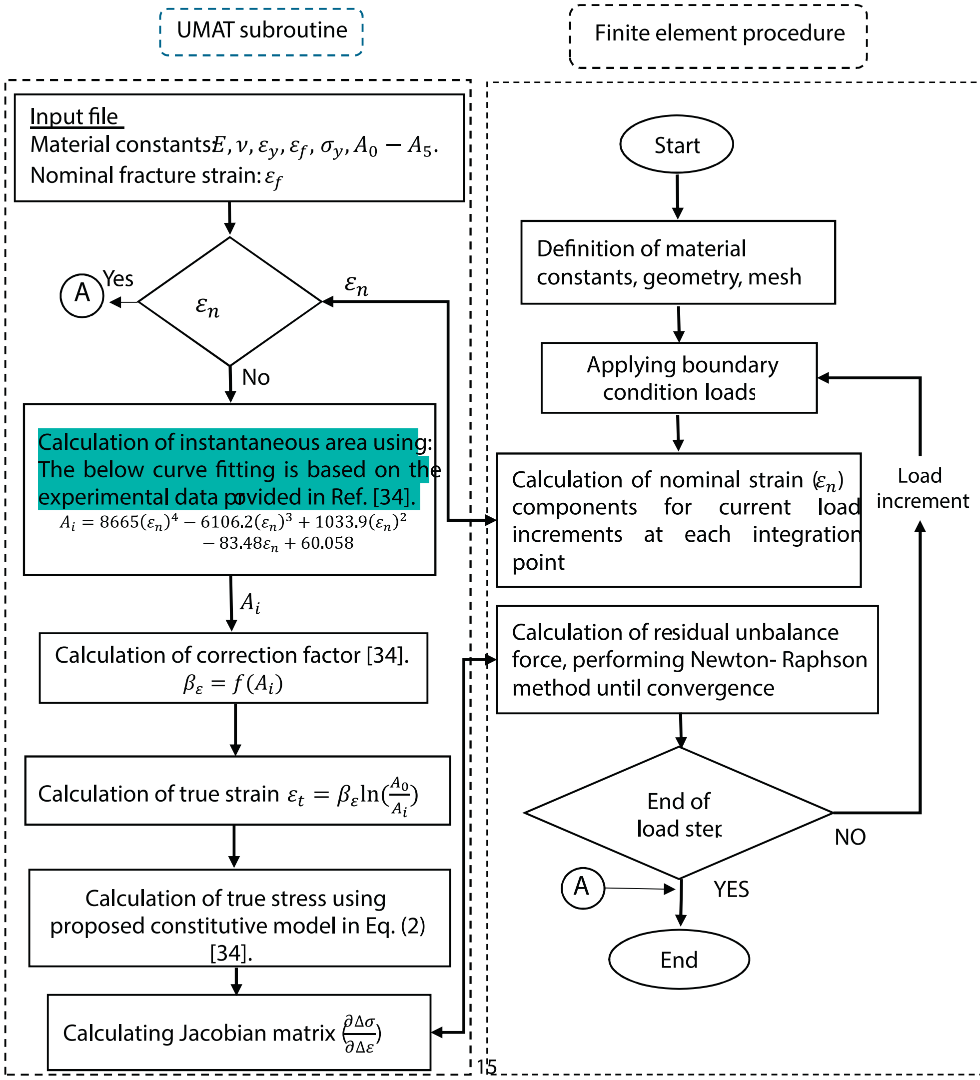

Fig. 7. FEM algorithm to define true stress-strain curve.

in Fig. 4a-b. For both cases, the maximum stress value (−80 MPa) is considered at the surface and the self-equilibration of the residual stress distribution is checked. The measurement based residual stress distributions are plotted as solid smooth lines, while the stepwise continuous lines represent the discontinuous residual stress distribution used in the layer-wise FE model.

In this modelling approach, several layers are created in the FE-model and the residual stress distributions are introduced to the FE analyses as temperature fields. The field distribution, field magnitude, and thermal expansion coefficient determine the temperature field. In the present study a thermal expansion coefficient of $\alpha = 1.2 \times 10^{-5}$, which is typical for steel, is used. The temperature field is applied to the initial undeformed mesh. Thus, the residual stress is implemented in FEM as thermal loading without any heat transfer between neighbor layers. The benefit of the global layer-wise modelling approach is that it automatically results in an equilibrium of stresses and strains. This results in excellent convergence between the modelled and estimated residual stress distributions after a few iteration steps. The difference between continuous and layer-wise modelling is that in the first approach, a continuous temperature distribution is used (a solid smooth line in Fig. 4) while in the layer-wise second approach, the temperature is constant in each layer following the estimated residual distribution (stepwise continuous lines in Fig. 4). Fig. 5a-b shows the comparison between the proposed layer-wise global modelling and two local modelling approaches called as layer-wise local model, and a continuous local line model. In the continuous local line model, the residual stress distribution was applied continuously in a specific region along three lines as illustrated in Fig. 5c. In the layer-wise local model, the

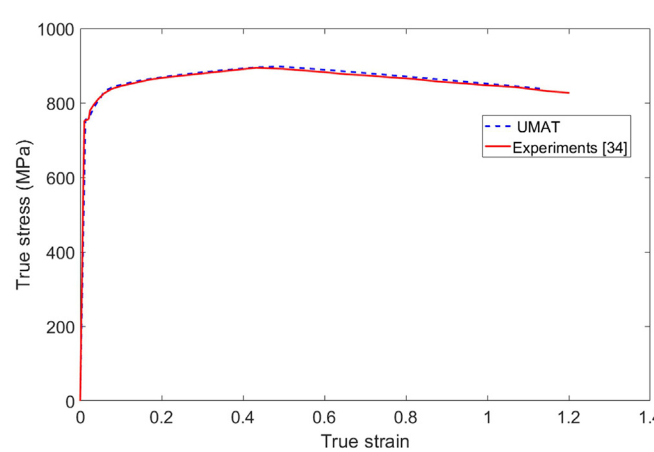

Fig. 8. True stress-strain curve of S690 in tensile uniaxial test.

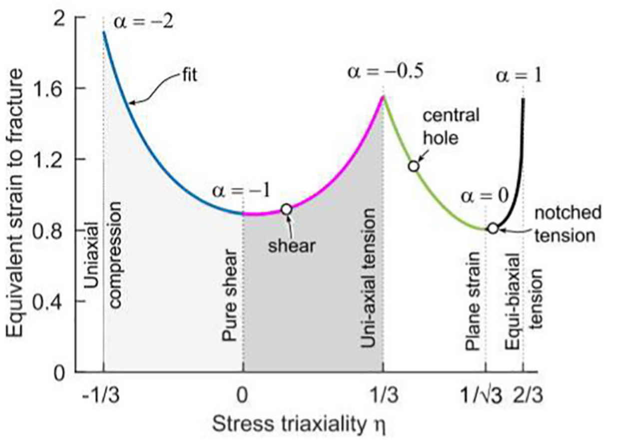

Fig. 9. Fracture locus for structural steel S235 calibrated with three different tensile tests [20,33].

residual stress distribution is modelled layer-wise but applied locally as depicted in Fig. 5b. It is worth to mention that the layer-wise approach is employed for two residual stress distributions (case 1 and case 2) in Fig. 5a and b as examples to highlight the applicability of the proposed model and the influence of measured residual stress distribution in defining the layers with constant temperatures.

The applied temperature field using different modelling approaches is depicted in Fig. 6a-c for estimated residual stress distribution of case 1. In the continuous local line approach, the temperature field is applied continuously along three lines in a specific local region containing the notch as shown in Fig. 6a. In the layer-wise approach, the local and global temperature field applied discontinuously with constant temperature in each layer following the initial distribution as depicted in Fig. 6b-c.

2.3. Damage model

Ductile fracture of metals is a complicated process, which is affected by the microstructure of the material, the stress and strain intensity, and

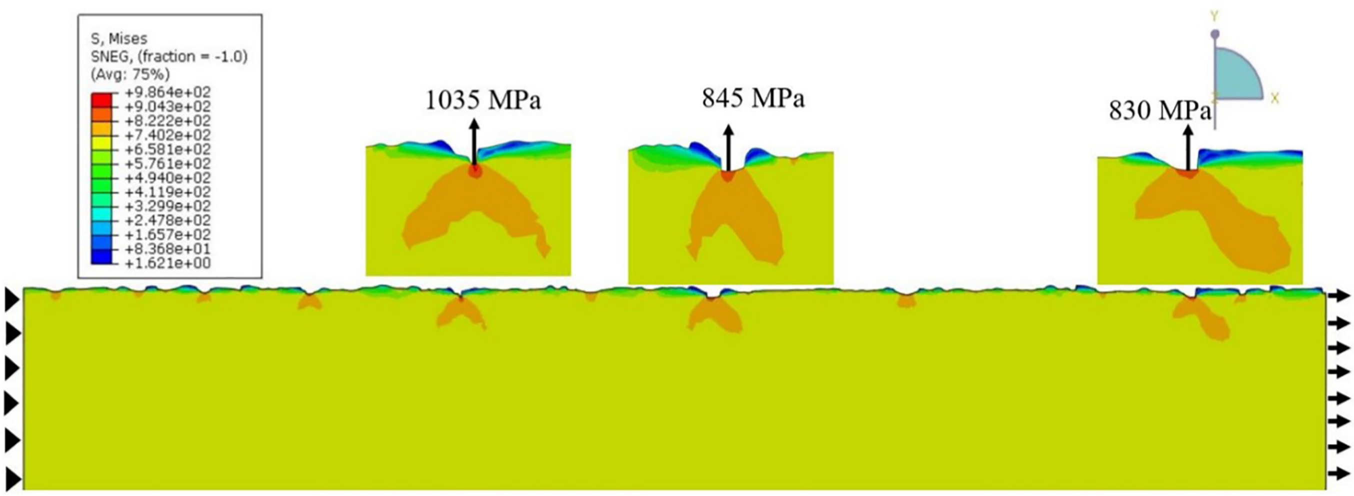

Fig. 10. The von-Mises stress distribution of the model.

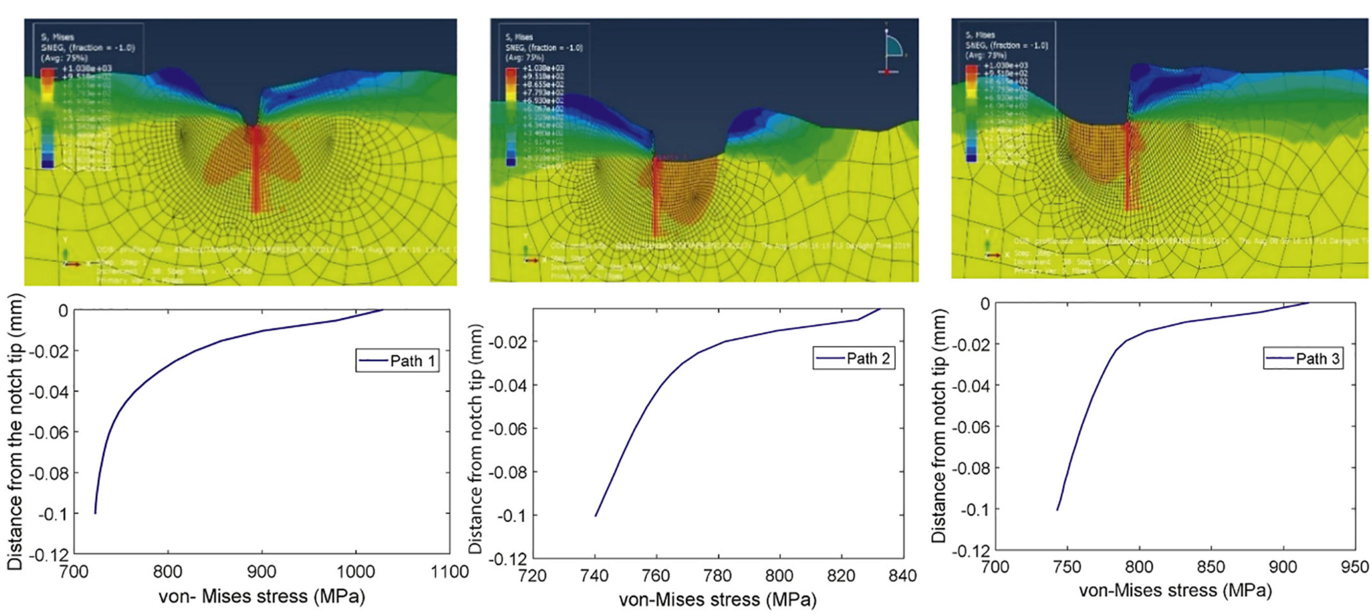

Fig. 11. The von-Mises stress gradient associated to three different micro-notches.

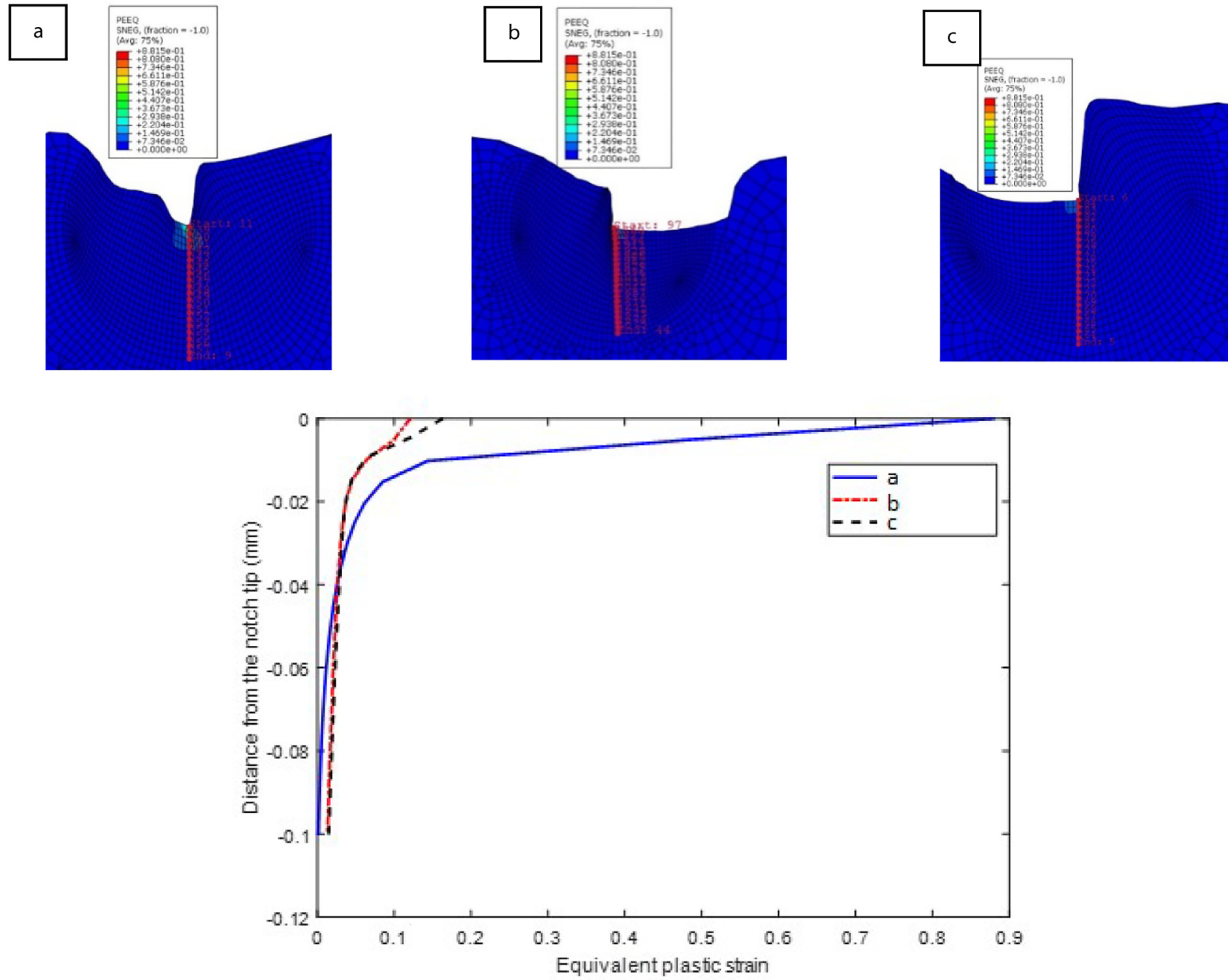

Fig. 12. Equivalent plastic strain gradient associated to three different micro-notches.

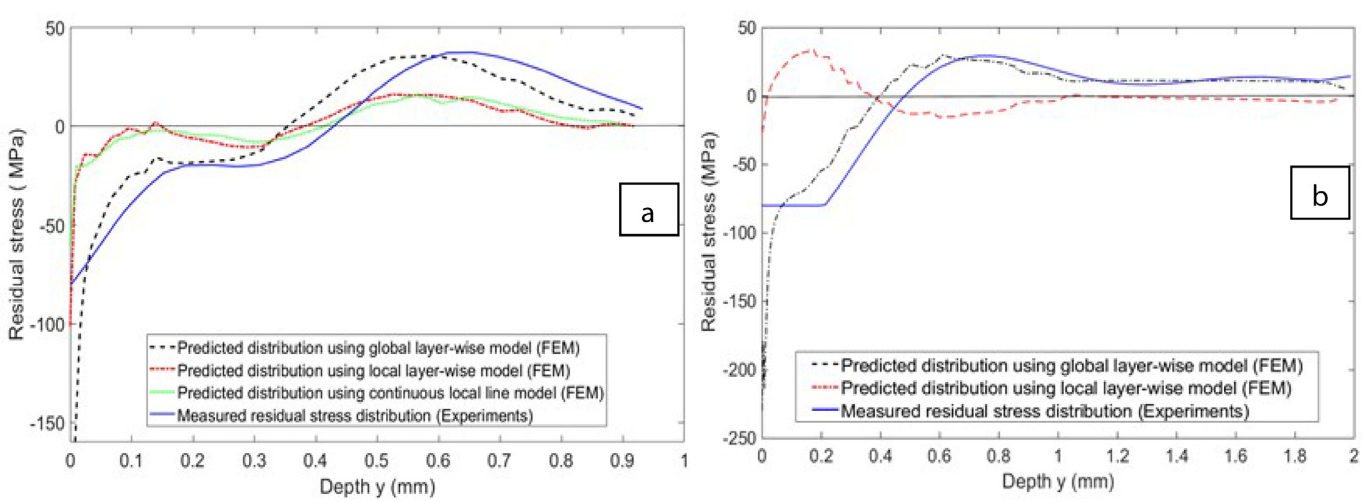

Fig. 13. Estimated and modelled residual stress distribution using two local modelling approaches and layer-wise global modelling approach for two different distributions, (a) case 1 and (b) case 2.

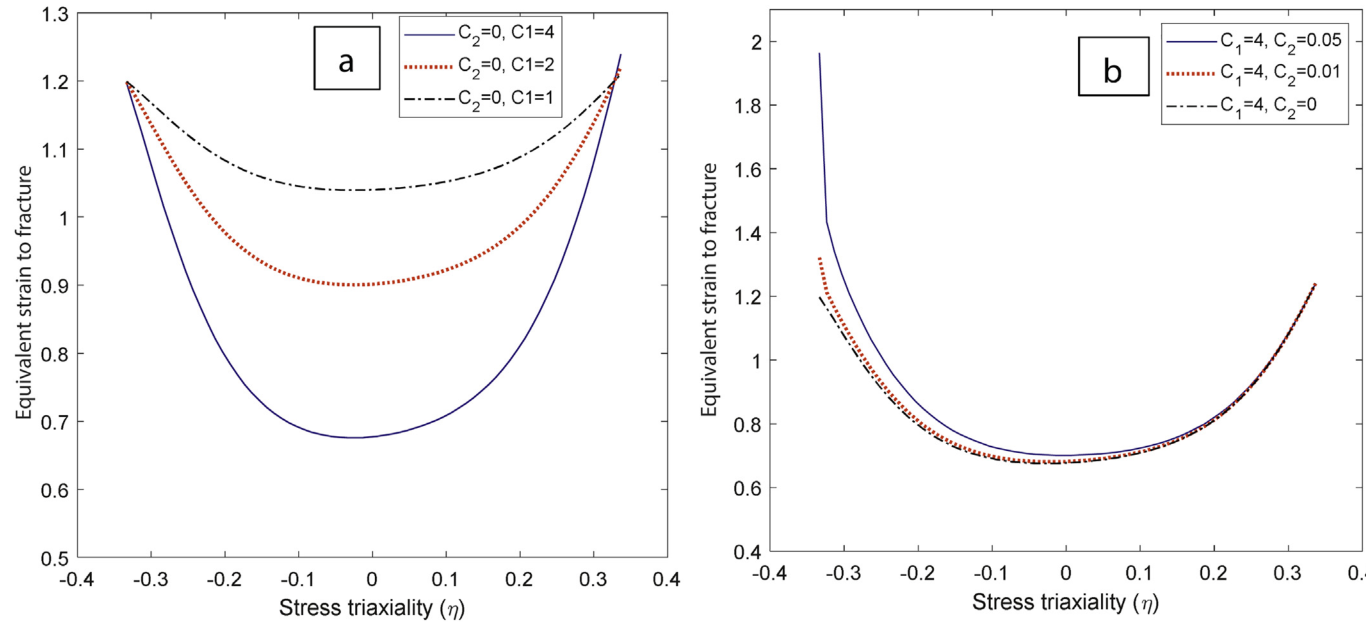

Fig. 14. Effect of (a) material constants C_1 and (b) material constants C_2 on the ductile fracture criterion ($C_3 = 1.2$).

the stress state defined by stress triaxiality, see e.g. [26,27]. In general, a ductile fracture in a metal sheet can be considered as a loss of stability. This phenomenon is also known as necking. At around the local area of the neck, the stress state becomes three-dimensional, as the material is in the plastic stage and high stress and strain gradients appear. The structural response under extreme loads involving ductile fracture is commonly determined with non-linear FE simulations. These simulations require the input of the true stress-strain ($\sigma_t - \varepsilon_t$) relation until the point of fracture initiation for defining fracture criterion [33]. This material behaviour is determined by the tensile test. In the context of a displacement controlled tensile test, fracture initiation is defined as the point followed by a sudden load drop resulting in the splitting of the specimen into two. The equivalent von Mises plastic strain at fracture initiation $\overline{\varepsilon_f}$ is denoted as the "fracture strain".

2.3.1. Equivalent plastic strain to fracture

In this study, a systematic approach is proposed to determine the fracture initiation strain and the equivalent stress-plastic strain material curve. This equivalent material curve is further extended to represent the whole damage process of the material, including necking, fracture initiation and propagation for micro-defects. The instantaneous area method has been employed to derive the true stress-strain curve for the high strength steel S690 [34]. The instantaneous area method is able to provide a full-range true stress-strain ($\sigma_t - \varepsilon_t$) curve based on measured instantaneous dimensions of the steel coupons. Owing to the use of the digital imaging correlation technique, instantaneous dimensions of the critical cross-sections of the steel coupons are continuously measured throughout the entire deformation history. Based on the assumption of constant volume in the steel coupons under large deformations, true strain, ε_t, is given as follows:

$$\varepsilon_t = \beta_\varepsilon \ln\left(\frac{A_0}{A_i}\right) \tag{1}$$

where A_0 is the original cross-sectional area; A_i is the measured instantaneous cross-sectional area and β_ε is a correction factor due to a non-uniform strain distributionwithin the cross section of the steel coupon.

Based on the corrected true stress-strain curves using the instantaneous area method, the constitutive model of the S690 high strength steel materials is proposed as follows to calculate true strain:

$$\sigma_t(\varepsilon)\begin{cases} \sigma_t = E\varepsilon_t & \text{for } \varepsilon_t \le \varepsilon_y \\ \sigma_t = f_y \times \left[1 + 3 \times 10^{-3} \times (\varepsilon_t/\varepsilon_y - 1)\right] & \text{for } \varepsilon_y \le \varepsilon_t \le 6\varepsilon_y \\ \sigma_t = f_y \times \left\{1.015 + 0.1 \times \left[1 - 0.01 \times \left(0.6\left(\frac{\varepsilon_t}{\varepsilon_y} - 6\right) - 10\right)^2\right]\right\} & \text{for } 6\varepsilon_y \le \varepsilon_t \le 15\varepsilon_y \\ \sigma_t = f_y \times \left\{1.094 + 0.1 \times \left(\frac{\varepsilon_t/\varepsilon_y - 15}{100}\right)^{0.45}\right\} & \text{for } 15\varepsilon_y \le \varepsilon_t \le 130\varepsilon_y \\ \sigma_t = f_y \times \left\{1.2 - 0.09 \times \left[\left(\frac{\varepsilon_t}{\varepsilon_y} - 130\right)^{1.1} / 340\right]\right\} & \text{for } 130\varepsilon_y \le \varepsilon_t \le 1.2 \end{cases} \tag{2}$$

where $E = 210$ MPa.

The process of this approach has been depicted in Fig. 7. Utilizing this approach, the true stress-strain curve of this material for the uniaxial

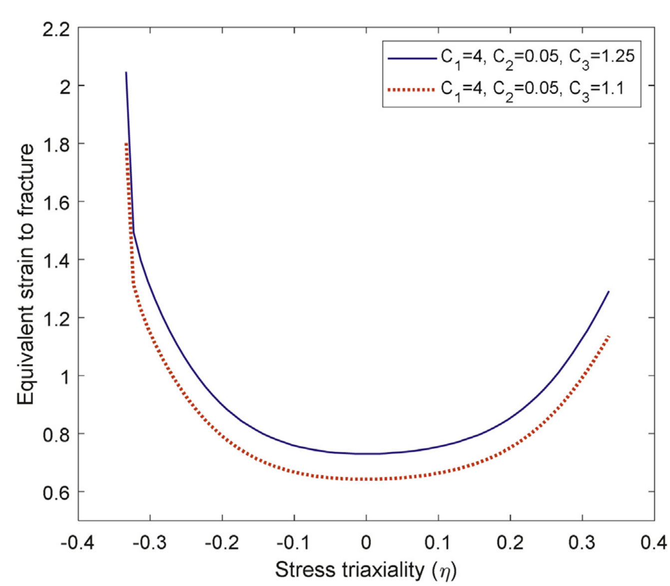

Fig. 15. Effect of material constants C_3 on the ductile fracture criterion.

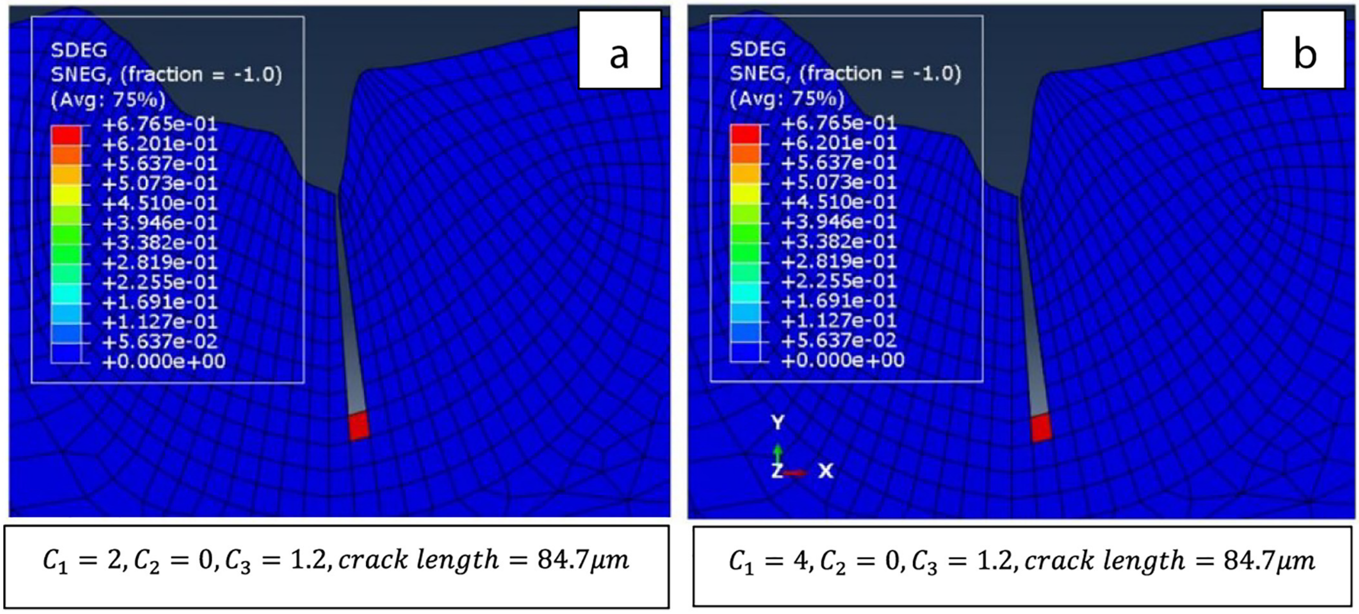

Fig. 16. FE simulation for two different fracture loci with constant values for C_2 and C_3 and varying values for C_1 (a) $C_1 = 2$, and (b) $C_1 = 4$.

test is shown in Fig. 8. This curve has been used then in FE simulation to calculate the equivalent von Mises plastic strain at fracture initiation.

2.3.2. Fracture criterion

In this section, the fracture criterion has been described using a fracture strain dependency on the stress triaxiality. Various calibration procedures for different fracture criteria have been presented in Ref. [35]. As an input, the adjustment framework requires a fracture locus in the space of stress triaxiality and fracture strain. An example of a commonly used fracture locus that is calibrated with several tensile tests is shown in Fig. 9.

Manufacturing of different kind of test specimens is very time-consuming and thus, damage model is selected so that it is suitable for calibration based on selected experiments. On this basis, the fracture locus is defined based on the fracture model [26], which is multiplication of the three damage accumulating models for nucleation, growth and shear coalescence of voids as follows:

$$\left(\frac{2\tau_{\max}}{\overline{\sigma}}\right)^{C_1} \times \left(\frac{\langle 1+3\eta \rangle}{2}\right)^{C_2} \times \overline{\varepsilon_f} = C_3 \langle x \rangle = \begin{cases} x & \text{when } x \geq 0 \\ 0 & \text{when } x < 0 \end{cases} \tag{3}$$

where η is the stress triaxiality, hydrostatic stress divided by equivalent von Mises stress. The model is based on the microscopic analysis of ductile fracture where void nucleation is described as a function of the equivalent plastic strain, void growth is a function of the stress triaxiality as $1 + 3\eta$, and void coalescence is controlled by the normalized maximal shear stress denoted as $\tau_{max}/\overline{\sigma}$. In this model, the material constant C_1 modulates the effect of the normalized maximal shear stress on the shear coalescence of voids during plastic deformation and C_2 modulates the effect of the stress triaxiality on the growth of voids. The material constant C_3 is equal to the equivalent plastic strain to fracture in uniaxial tension. Although the model can describe these different phenomena, one of the reasons to prefer this criterion is that the shape of the fracture locus can be easily controlled with the three material constants. Furthermore, we stress that Eq. (3) gives the fracture strain for the full range of stress triaxiality, but the focus in the current study is on the region corresponding to uniaxial stretching: from the uniaxial compression ($\eta = -1/3$) until the uniaxial tension ($\eta = 1/3$).

Ideally, the input fracture criterion $\overline{\varepsilon_f}$ in Eq. (3) should be determined on the basis of tests covering the full stress triaxiality range. For instance, in the study where the fracture model was proposed [26] the material constants C_1, C_2 and C_3, were obtained by fitting a curve to the experimental results. The same approach is used, but only uniaxial tension test data together with single peak load tensile are utilized. The input fracture criterion in the uniaxial tension range is calibrated based on calculated equivalent plastic strain at fracture initiation, failure strain $\overline{\varepsilon_f}$. The value for material constant C_3 is 1.2 which gives the $\overline{\varepsilon_f}$ at uniaxial tension $\eta = 1/3$. Then different values for C_1, C_2 have been set based on the common range ($1 < C_1 < 8$ and $0 < C_2 < 1$) for these parameters [26]. The sensitivity analyses should be carried out to study the effects of C_1, C_2 parameters on the micro-carck formation and crack length utilizing varied fracture locus defined based on different values of these two parameters in the FE simulation. Then, using an inverse numerical-experimental approach C_1, C_2 can be calibrated in such a way that FE simulation for pre-notched specimens with ductile

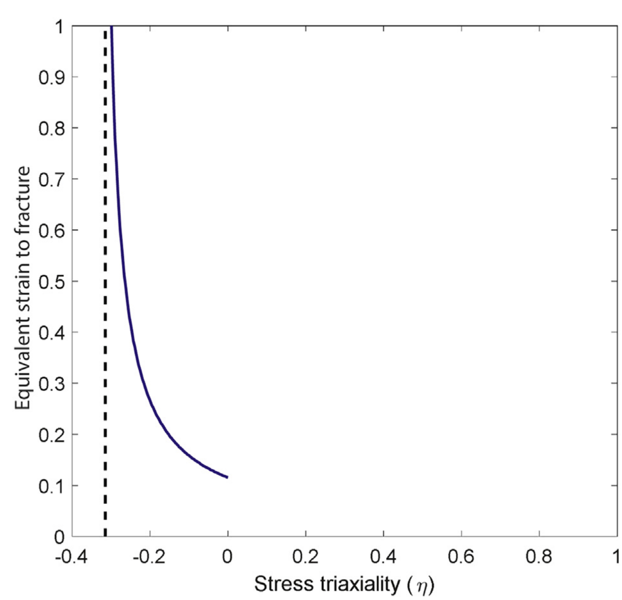

Fig. 17. The relationship of fracture strain and stress triaxiality [36].

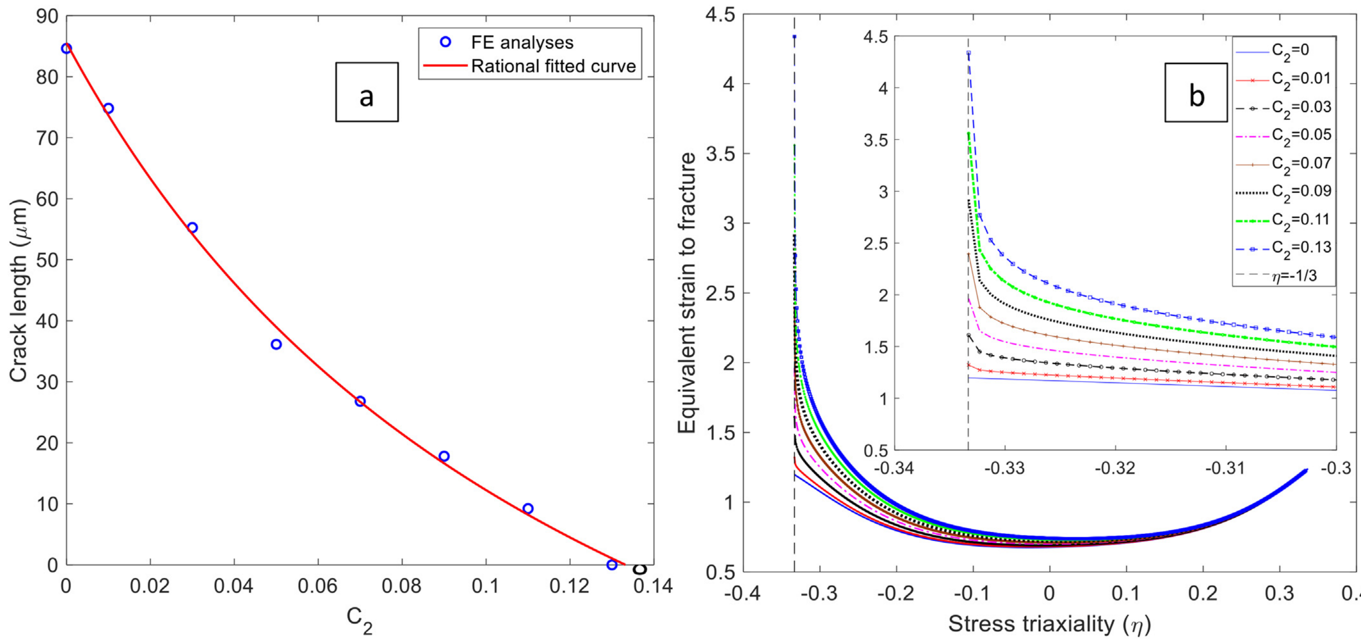

Fig. 18. An example of micro-crack length based calibration curve using FEM simulation for material constant C_2, (a) the effect of material constants C_2 on the crack size and (b) the corresponding fracture strain at stress triaxiality $\eta = -1/3$ for different C_2 values with $C_1 = 1.2$, $C_2 = 4$.

damage can predict the micro-crack observed from SEM images in the vicinity of the notch under peak load conditions.

3. Results and discussion

To verify the introduced approach, it is applied to sandblasted 690 high strength steel plate specimen as a case study. FE simulations were carried out on the model considering the combined effects of surface roughness and residuals stress according to the load and boundary conditions applied in the experimental conditions. A damage model based on the microscopic analysis of ductile fracture is employed in the FE simulation to investigate the possibility of crack initiation in the vicinity of critical micro notches generated by the surface roughness. A special approach is proposed for the calibration of the damage model's material parameters based on micro-crack development using FE simulation.

3.1. Gradient at the notch tip

Due to the complexity of the surface topology, high local stresses occur in the root of the in the largest micro-defects as shown in Fig. 10. The figure shows the von-Mises stress distribution of the actual surface topography after peak load tests without considering the material damage. The maximum von-Mises stress concentrates at several surface micro-defects or micro-notches generated by the surface roughness of the model, and the maximum value is located at the root of the deepest and sharpest defect. It can be seen that the maximum von-Mises stress in this area presents a butterfly-shaped radial distribution. The element mesh size and quality are especially well defined in the most critical locations; see Fig. 11 and Fig. 12. These figures show the von-Mises stress and equivalent plastic strain gradients for the three largest micro-defects, which are considered as a potential site for damage initiation, and then micro-cracking formation.

3.2. Residual stress distribution

The predicted residual stress distribution for each case of Fig. 4a-b is depicted in Fig. 13a-b using the proposed layer-wise global modelling and the two local modelling approaches. The layer-wise global modelling approach has been applied for the whole surface and the local modelling approaches have employed for the most three critical notches as shown in Fig. 10. It can be seen that the global modelling approach is relatively insensitive to the free surface profile and it follows the estimated input distribution better than local modelling approaches after the first iteration loop. To get an exact fit it is necessary to have an iterative modelling approach where the temperature field is modified according to the difference of the fit. This is due to fact that the surface roughness and layer-wise residual stress distribution effect the self-balancing equilibrium of applied residual stress field.

For further analyses in this study, the residual stress has been considered in the FE simulation using layer-wise global modelling for case 2.

3.3. Fracture locus calibration

The sensitivity analyses have been carried out to investigate the effects of the material constants C_1, C_2, and C_3 on the ductile fracture criterion and then micro-crack formation in the FE simulation. Fig. 14a-b shows the example of calibrated fracture locus for different values of C_1 and C_2, respectively.

The material constant C_1 modulates the effect of the normalized maximal shear stress on the shear coalescence of voids during plastic deformation. As C_1 becomes large, the influence of the maximal shear stress on ductile fracture increases and accordingly, the fracture strain is reduced. The material constant C_1 adjusts the ratio of the equivalent plastic strain to fracture in the uniaxial tension to that in the pure shear strain. As discussed above, the voids start to coalesce with the other after they grow up to a certain size. Power exponent C_2 is added on the function of voids growth to represent void coalescence. Therefore, if parameter C_2 increases, 'voids growth in compression' will be largely suppressed and the progress of voids growth under shear stress

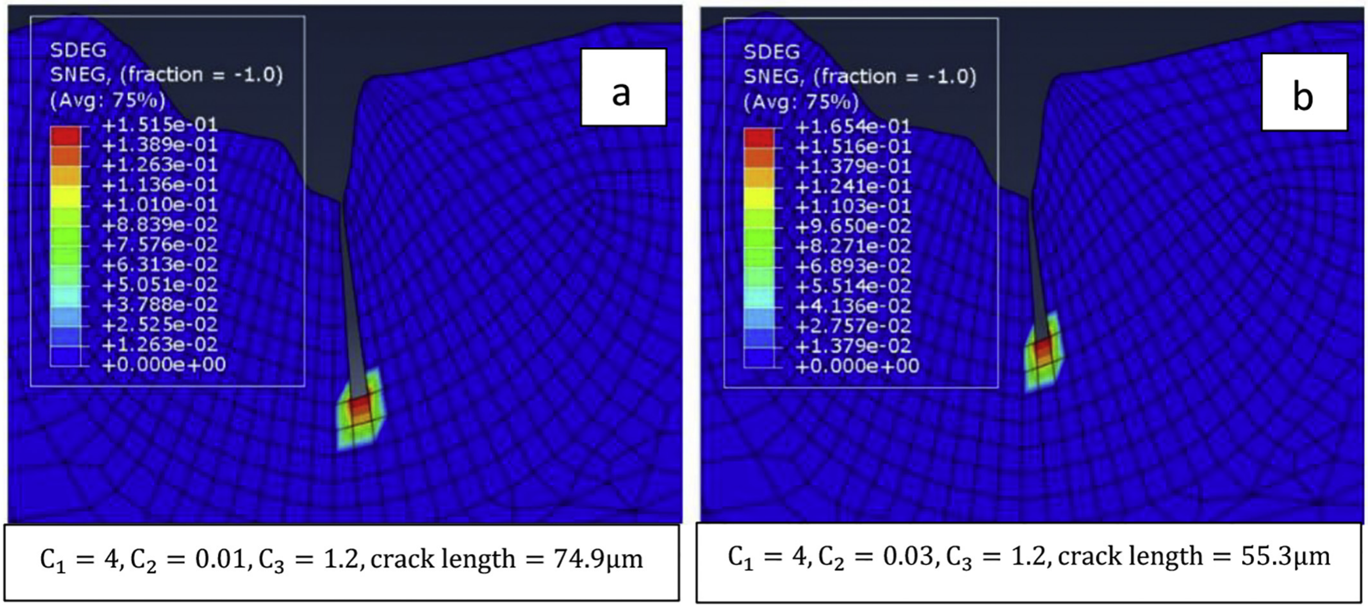

Fig. 19. FE simulation for two different fracture loci with varying C_2 values (a) $C_2 = 0.01$, and (b) $C_2 = 0.03$.

will be slower and voids coalescence will be distinct in compression. For negative stress triaxialities, the fracture is governed by shear mode.

The role of the material constant C_3 is quite simple compared with the roles of C_1 and C_2. It simply varies the magnitude of the fracture locus diagram with no influence on the shape as presented in Fig. 15.

After the role of material constants (C_1, C_2, C_3) on the ductile fracture criterion have been investigated, we can define the appropriate fracture locus for this material using the uniaxial tension test data, available experimental trends for fracture locus in literature and experimental data showing crack growth after one cycle with the peak load effect. As explained before, C_3 represents the equivalent plastic strain at fracture initiation, $\overline{\varepsilon_f}$, at uniaxial tension $\eta = 1/3$. This is obtained from uniaxial tension test data and introduced to the numerical simulation to present the true stress-strain curve using the instantaneous area method. The calibration of C_1, presenting the ratio of the equivalent plastic strain to fracture in the uniaxial tension to that in the pure shear strain, is defined based on the earlier experimental observations and sensitivity analysis. In this study, a common mean value,

$C_1 = 4$, is observed to give a reliable estimation for surface integrity analysis since the surface has negative residual stress and micro-defects, and thus, the damage occurs mainly in the compression side of the fracture locus. In this case, the damage induced micro-crack formation is insensitive to the values of C_1 as shown in Fig. 16a-b.

As the last step, material constant C_2 as the most affecting material constant is calibrated. Constant C_2 values determine the equivalent plastic strain to fracture at negative stress triaxiality. Bao and Wierzbicki found if the equivalent plastic strain to fracture would be very large, the fracture near stress triaxiality $\eta = -1/3$ is very hard to happen [36]. Indeed, the fracture strain asymptote to $\eta = -1/3$ with large values as depicted in Fig. 17. However, at this point ($\eta = -1/3$) due to the shape change of voids, the interaction of the void free area fraction along the maximum shear stress direction and the magnitude of the maximum shear stress, shear coalescence of voids form a fracture surface.

Thus, the uniaxial compressive peak load test for the original surface topography can provide necessary information of micro-cracking (micro-crack length) required for calibration of constant C_2. When the micro-crack length for selected peak load level(s) is available from experiments, the constant C_2 can be determined with FEM simulations. Based on FE analysis, the micro-crack length as a function of constant C_2 values can be defined for these load levels. Then a calibration curve can be created. Fig. 18 shows an example of this kind of curve for the sandblasted high strength steel material. For this material, the other material constants ($C_1 = 4, C_3 = 1.2$) were kept constant and only the constants C_2 were varied between 0 and 0.13 to define different fracture loci. Then, the FE simulations have been carried out to compute the micro-crack length. Fig. 18a depicts the effect of C_2 values on the crack size due to ductile damage under peak load conditions. Fig. 18b shows the corresponding fracture loci for different C_2 values. Increasing C_2 values results in decreasing the size of the crack. The voids' growth in compression ($\eta = -1/3$) has been largely suppressed and the progress of voids' growth under shear stress is slower. Therefore, C_2 values can be calibrated in such a way that the fracture strain asymptote to $\eta = -1/3$ does not have large values.

Then, the correct value for constant C_2 was selected based on the micro-crack length obtained from microscopic analysis of the surface. When the micro-crack length was known, the calibration of the constants C_2 was easy since the formed micro-crack length is sensitive for the constant C_2; see Fig. 19.

The experimental observation of the micro-crack length from SEM images after overload shows the shear coalescence of voids and ductile crack formation as depicted in Fig. 20. Thus, C_2 is calibrated in such a way that FE simulation with ductile damage can predict the crack initiation and propagation under peak load conditions.

It is worth to mention that further experimental study can be carried out to define a systematic approach for C_2 parameter calibration using different overloads for pre-notched specimens and the sensitivity of the proposed approach in micro-crack formation with respect to C_2 values. The crack size can then be compared with FE simulation with varying C_2 parameter to find appropriate C_2 value predicting similar size with experiments. This calibration approach to defining the fracture locus of the material is more simple and straightforward in comparison with the experimental circumstance proposed by Bao and Wierzbicki [37] using tension tests employing round bars with or without notch as well as tension tests using notched plate specimens, simple shear tests [38,39] and compression tests. Since the material parameter calibration for the damage model can be carried out based on the micro-crack development, the proposed approach

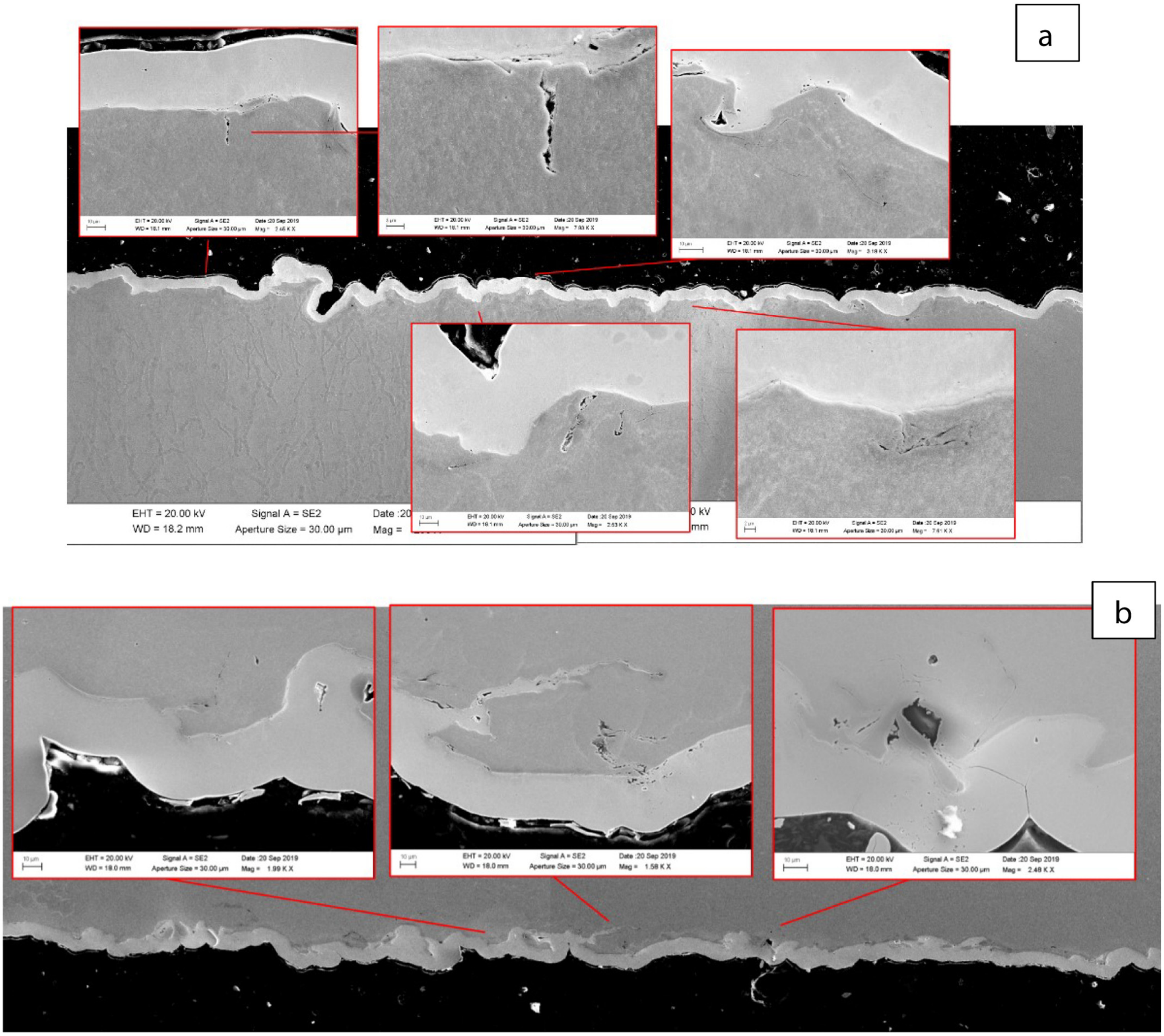

Fig. 20. The SEM Images from (a) the top and (b) the bottom side of the specimen after overload.

requires fewer effort for the geometrical designs of the specimens. Moreover, the use of standard specimen is a great challenge for investigation of the thin affected material zone that can be eliminated by the proposed approach.

Utilizing the calibration process and sensitivity analyses described in this section, the material constants $C_1 = 4$, $C_2 = 0.01 - 0.03$, $C_3 = 1.2$ have been obtained to define the fracture locus for modelling progressive damage and failure of ductile metal in this FEM analyses for high strength steel S690. It is worth mentioning that damage models have been widely applied on a bigger scale but not for micro-defects and surface. The proposed approach for material parameters calibration of the damage model based on micro-crack development has not been employed so far and it can be applied as a generic approach for engineering materials. In the future work, an investigation will be carried out to characterize the effects of an initial peak load on the geometrical parameters, residual stress state and crack size using the obtained fracture locus for high strength steel S690.

It should be noted that the compressive loads tend to relax compressive residual stresses in proportion to their magnitude. Surface roughness as an affecting parameter on the local stress concentration influences the relaxation behaviour. This numerical simulation can consider and determine the residual stress relaxation; however, further study is required to systematically analyze the sensitivity of the crack formation and damage mechanism to residual stress relaxation. The future track of this work will focus on providing a holistic understating of the role of the residual stress relaxation rate and compressive peak loading on the crack formation.

4. Conclusion

In this study, a new FEM approach has been developed to account for the influences of surface roughness, residual stress, and material effect simultaneously on the formation of micro-cracks. A layer-wise residual stress modelling and a ductile fracture criterion with a special calibration approach were introduced. A ductile fracture criterion is introduced for the prediction of damage initiation and evolution. The fracture locus is reconstructed using a calibration procedure to obtain the effective material constants in the criterion. Furthermore, different approaches for residual stress modelling are compared. The main findings of this investigation can be concluded as follows:

- The residual stress should be applied globally using the developed multiple layer modelling approach, with a constant temperature at each layer in such a way that it follows the estimated residual stress distribution. This approach robustly models the residual stress without a significant amount of iteration and avoids the uncertainties and complexities involved in the FE modelling for residual stress simulation.
- An inverse numerical-experimental approach is introduced to calibrate a ductile fracture criterion to describe the material failure under different stress states. Uniaxial tensile test and micro cark formation from micro-defect material surface are utilized. The calibrated ductile fracture criterion is successfully applied to predict the fracture locus of high strength steel.
- The developed FEM approach, considering the material and residual stress effects together with damage mechanism, can provide holistic understating about the role of surface roughness on the crack formation under peak load conditions. Stress gradient and equivalent plastic strain at the notch tip, and ductile fracture criteria specify the critical notch for damage and crack formation.
- The proposed modelling principles and calibration approach can be employed for other materials and surface profiles.

Author statement

Prof. Jairan Nafar Dastgerdi contributed to the paper by methodology, investigation, data analysis, and writing the original draft. Fariborz Sheibanian contributed to the paper by numerical modeling. Prof Heikki Remes contributed to the paper by conceptualization and giving valuable comments and suggestions. Dr. Pauli Lehto contributed to the paper by experimental validation. Prof. Hossein Hosseini Toudeshky contributes to the paper by giving valuable comments and suggestions.

Declaration of Competing Interest

None.

Acknowledgements

The present research was financially supported by project RAMSSES that has received funding under the European Union's Horizon 2020 research and innovation programme under the grant agreement No 723246. The information contained herein reflects the views only of the authors, and the European Union cannot be held responsible for any use which may be made of the information contained herein. All the financial support is gratefully appreciated.

References

[1] Y.K. Gao, X.B. Li, Q.X. Yang, et al., Influence of surface integrity on fatigue strength of 40CrNi2Si2MoVA steel, Mater. Lett. 61 (2) (2007) 466–469.
[2] S.A. McKelvey, A. Fatemi, Surface finish effect on fatigue behavior of forged steel, Int. J. Fatigue 36 (2012) 130–145.
[3] L.I. Xun, C. Guan, P. Zhao, Influences of milling and grinding on machined surface roughness and fatigue behavior of GH4169 superalloy workpieces, Chin. J. Aeronaut. 6 (2018) 1399–1405.
[4] S.G. Crool, Surface roughness profile and its effect on coating adhesion and corrosion protection: a review, Prog. Org. Coat. 148 (2020) 105847.
[5] H. Remes, E. Korhonen, P. Lehto, J. Romanoff, S. Ehlers, A. Niemela, P. Hiltunen, T. Kotakanen, Influence of surface integrity on fatigue strength of high-strengh steel, J. Constr. Steel Res. 89 (2013) 21–29.
[6] I. Lillemae-Avi, S. Liinalampi, E. Lehtimalil, H. Remes, P. Lehto, J. Romanoff, S. Ehlers, A. Niemela, Fatigue strength of high strength steel after shipyard production process of plasma cutting, grinding and sandblasting, Weld World 62 (2018) 1273–1287.
[7] P. Diekhoff, J. Hensel, Th. Nitschke, K. Dilger, Investigation on fatigue strength of cut edges produced by various cutting methods for high-strength steels, Weld World 64 (2020) 545–561.
[8] A. Haghshenas, M.M. Khonsari, Damage accumulation and crack initiation detection based on the evolution of surface roughness parameters, Int. J. Fatigue 107 (2018) 130–144.
[9] J.J. Wang, Z.X. Wen, X.H. Zhang, Y.C. Zhao, Z.F. Yue, Effect mechanism and equivalent model of surface roughness on fatigue behavior of nickel-based single crystal superalloy, Int. J. Fatigue 125 (2019) 101–111.
[10] S. Singh, H. Singh, S. Chaudhary, R.K. Buddu, Effect of substrate surface roughness on properties of cold-sprayed coppercoatings on SS316L steel, Surf. Coat. Technol. 389 (2020) 125619.
[11] F. Paknahad, F. Sahriari Nogorani, Effects of substrate roughness on the surface morphology and corrosion properties of Fe- and Ni-aluminide coatings on martensitic stainless steel, Surf. Coat. Technol. 392 (2020) 125761.
[12] A. Alhussein, J. Capelle, J. Gilgert, A. Tidu, S. Hariri, Z. Azari, Static, dynamic and fatigue characteristics of the pipeline API 5L X52 steel after sandblasting, Eng. Fail. Anal. 27 (2013) 1–15.
[13] S. As, B. Skallerud, B. Tveiten, Surface roughness characterization for fatigue life predictions using finite element analysis, Int. J. Fatigue 30 (12) (2008) 2200–2209.
[14] M. Zhang, W.Q. Wang, P.F. Wang, et al., The fatigue behavior and mechanism of FV520B-I with large surface roughness in a very high cycle regime, Eng. Fail. Anal. 66 (2016) 432–444.
[15] J. Pegues, M. Roach, R. Scott Williamson, et al., Surface roughness effects on the fatigue strength of additively manufactured Ti-6Al-4V, Int. J. Fatigue 116 (2018) 543–552.
[16] P.S.C.P.D. Silva, L.C. Campanelli, C.A.E. Claros, et al., Prediction of the surface finishing roughness effect on the fatigue resistance of Ti-6Al-4V ELI for implants applications, Int. J. Fatigue 103 (2017).
[17] M. Suraratchai, J. Limido, C. Mabru, et al., Modelling the influence of machined surface roughness on the fatigue life of aluminium alloy, Int. J. Fatigue 30 (12) (2008) 2119–2126.
[18] M. Storheim, J. Amdahl, I. Martens, On the accuracy of fracture estimation in collision analysis of ship and offshore structures, Mar. Struct. 44 (C) (2015) 254–287.
[19] M.A.G. Calle, M. Alves, A review-analysis on material failure modeling in ship collision, Ocean Eng. 106 (C) (2015) 20–38.
[20] M. Kõrgesaar, The effect of low stress triaxialities and deformation paths on ductile fracture simulations of large shell structures, Mar. Struct. 63 (2019) 45–64.
[21] X. Zhuang, T. Wang, X. Zhu, Z. Zhao, Calibration and application of ductile fracture criterion under non-proportional loading condition, Eng. Fract. Mech. 165 (2016) 39–56.
[22] J. Papasidero, V. Doquet, D. Mohr, Ductile fracture of aluminum 2024-T351 under proportional and non-proportional multi-axial loading: Bao–Wierzbicki results revisited, Int. J. Solids Struct. 69–70 (2015) 459–474.
[23] Z. Xue, M.G. Pontin, F.W. Zok, J.W. Hutchinson, Calibration procedures for a computational model of ductile fracture, Eng. Fract. Mech. 77 (2010) 492–509.
[24] Y. Lou, H. Huh, Prediction of ductile fracture for advanced high strength steel with a new criterion: experiments and simulation, J. Mater. Process. Technol. 213 (2013) 1284–1302.
[25] Y.S. Lou, H. Huh, Extension of a shear controlled ductile fracture model considering the stress triaxiality and the lode parameter, Int. J. Solids Struct. 50 (2013) 447–455.
[26] Y. Lou, H. Huh, S. Lim, K. Pack, New ductile fracture criterion for prediction of fracture forming limit diagrams of sheet metals, Int. J. Solids Struct. 49 (2012) 3605–3615.
[27] Q. Hu, X. Li, X. Han, J. Chen, A new shear and tension based ductile fracture criterion: Modeling and validation, Eur. J. Mech. A-Solids 66 (2017) 370–386.
[28] D. Mohr, S.J. Marcadet, Micromechanically-motivated phenomenological Hosford–Coulomb model for predicting ductile fracture initiation at low stress triaxialities, Int. J. Solids Struct. 67–68 (2015) 55.
[29] SFS-EN ISO 4288, Geometrical Product Specifications (GPS) — Surface Texture: Profile Method — Rules and Procedures for the Assessment of Surface Texture, 1996.
[30] W.J. Cheong, B.L. Luan, D.W. Shoesmith, The effects of stabilizers on the bath stability of electroless Ni deposition and the deposit, Appl. Surf. Sci. 229 (2004) 282–300.
[31] EN ISO 15305:2008, Non-Destructive Testing–Test Method for Residual Stress Analysis by X-ray Diffraction, 2008.
[32] S. Lestari, Residual Stress Measurements of Unblasted and Sandblasted Mild Steel Specimens Using X-Ray Diffraction, Strain-gage Hole Drilling, and Electronic Speckle Pattern Interferometry (ESPI) Hole Drilling Methods, University of New Orleans, 2004 90 Theses and Dissertations.
[33] M. Kõrgesaar, J. Romanoff, H. Remes, P. Palokangas, Experimental and numerical penetration response of laser-welded stiffened panels, Int. J. Impact Eng. 114 (2018) 78–92.
[34] H.C. Hoa, K.F. Chunga, X. Liua, M. Xiaoa, D.A. Nethercot, Modelling tensile tests on high strength S690 steel materials undergoing large deformations, Eng. Struct. 192 (2019) 305–322.
[35] T. Wierzbicki, Y. Bao, Y.W. Lee, Y. Bai, Calibration and evaluation of seven fracture models, Int. J. Mech. Sci. 47 (2005) 719–743.
[36] Y. Bao, T. Wierzbicki, On the cut-off value of negative triaxiality for fracture, Eng. Fract. Mech. 72 (2005) 1049–1069.
[37] Y.B. Bao, T. Wierzbicki, On fracture locus in the equivalent strain and stress triaxiality space, Int. J. Mech. Sci. 46 (2004) 81–98.
[38] Z.M. Yue, C. Soyarslan, H. Badreddine, et al., Identification of fully coupled anisotropic plasticity and damage constitutive equations using a hybrid experimental-numerical methodology with various triaxialities, Int. J. Damage Mech. 24 (2014) 683–710.
[39] X. Zhuang, T. Wang, X. Zhu, Z. Zhao, Calibration and application of ductile fracture criterion under non-proportional loading condition, Eng. Fract. Mech. 165 (2016) 39–56.